

Fig. 1. Radial profiles across an initially 2-km-high and 150-km-radius plateau. The plateau and upper 2.5 km of the crust are of diabase composition and the lower 2.5 km of crust is of gabbro and overlies a peridotite mantle. The lithosphere is 33 km thick. The thermal gradient through the upper crust is 28 K km^{-1} . Topographic profiles are shown for the original plateau, the instantaneous elastic response to loading (isostatic balance), and for 0.5, 10, 50, and 500 Ma. Vertical exaggeration is $\times 21$.

from those of other workers in that (1) our thermal models are distinctive and we believe more realistic and (2) our models are dynamically isostatically balanced with both hydrostatic restoring forces and dynamic support by tectonic stress and basal tractions being modeled. The implications of our models' stress evolution for surface deformation can be tested against Magellan imagery.

References: [1] Melosh H. J. and Raefsky A. (1980) *Geophys. J. R. Astron. Soc.*, 60, 333–354. [2] Phillips R. J. et al. (1992) *LPSC XXXIII*, 1065–1066. [3] Solomon S. C. and Head J. W. (1984) *JGR*, 87, 9236–9246. [4] Phillips R. J. and Malin M. C. (1984) *Annu. Rev. Earth Planet. Sci.*, 12, 411–443.

N93-14314

484228

FLEXURAL ANALYSIS OF UPLIFTED RIFT FLANKS ON VENUS. Susan A. Evans, Mark Simons, and Sean C. Solomon, Department of Earth, Atmospheric, and Planetary Sciences, Massachusetts Institute of Technology, Cambridge MA 02139, USA.

Introduction: Knowledge of the thermal structure of a planet is vital to a thorough understanding of its general scheme of tectonics. Since no direct measurements of heat flow or thermal gradient are available for Venus, most estimates have been derived from theoretical considerations or by analogy with the Earth [1]. The flexural response of the lithosphere to applied loads is sensitive to regional thermal structure. Under the assumption that the yield strength as a function of depth can be specified, the temperature

gradient can be inferred from the effective elastic plate thickness [2]. Previous estimates of the effective elastic plate thickness on Venus range from 11–18 km for the foredeep north of Uorsar Rupes [3] to 30–60 km for the annular troughs around several coronae [4,5]. Thermal gradients inferred for these regions are $14\text{--}23 \text{ K km}^{-1}$ and $4\text{--}9 \text{ K km}^{-1}$ respectively [3,4]. In this study, we apply the same techniques to investigate the uplifted flanks of an extensional rift. Hypotheses for the origin of uplifted rift flanks on Earth include lateral transport of heat from the center of the rift, vertical transport of heat by small-scale convection, differential thinning of the lithosphere, dynamical uplift, and isostatic response to mechanical unloading of the lithosphere [6]. The last hypothesis is considered the dominant contributor to terrestrial rift flanks lacking evidence for volcanic activity, particularly for rift structures that are no longer active [6]. In this study, we model the uplifted flanks of a venusian rift as the flexural response to a vertical end load.

Tectonic Environment: We examine a linear rift system centered at 33°S , 92°E , in an area to the east of Aino Planitia. The feature appears as a linear ridge in Pioneer Venus altimetry and thus has been named Juno Dorsum. However, the increased resolution of Magellan images and topography has established that this feature is actually a linear rift with pronounced flanking highs. The rift is 100 km wide and 450 km long; it has a central depression 1–2 km deep and flanks elevated by as much as 1 km (Figs. 1 and 2). The rift connects a 1.5-km-high volcano on its western edge to two coronae, Tai Shan and Gefjun [7], to the east. Despite the presence of the volcano and coronae, both the center of the rift and the adjacent flanks appear to be free of volcanic flows. Juno Dorsum is at the end of a nearly continuous chain of coronae, rifts, and linear fractures that extends eastward and appears to terminate at the northwestern edge of Artemis Corona. The rift appears in Magellan images as numerous east-northeast-trending lineaments, which we interpret to be normal faults. To the north and south are smooth, radar-dark plains that stand very close to mean planetary elevation.

We use Magellan altimetric profiles from orbits 965–968 and 970–972 (Figs. 1 and 2). While topographic profiles perpendicular to the strike of the rift are preferable, the orbit tracks cross the rift

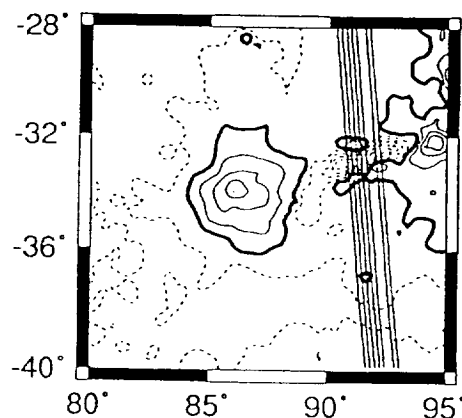


Fig. 1. Topographic contour map of the Juno Dorsum region. Thin solid lines denote positive elevation contours, thick solid lines zero elevation, and dashed lines negative elevations. The contour interval is 0.3 km, and the datum is mean planetary radius, 6051.9 km. The rift is located in the center right of the figure, with an unnamed volcano to its west. The north-south-trending lines indicate the tracks of orbits 965–968 and 971–972 (numbers increasing eastward). The orbit tracks make an angle of approximately 75° with the strike of the rift.

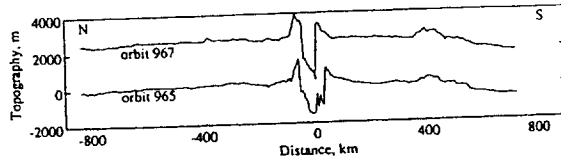


Fig. 2. Example orbit profiles over Juno Dorsum; see Fig. 1 for location. The rift flanks are elevated 800 to 1000 m above the surrounding plains, and interference from other regional topographic features is minimal. Orbit 967 has been offset vertically by 2500 m for clarity.

at an angle of approximately 75° , and we can easily make the geometrical correction for this small difference. Profiles from single orbits avoid errors introduced by interorbit offsets. As is evident in Fig. 2, the topography of the surrounding plains region is rather smooth, and the uplift of the flanks is quite distinct and easy to discern from other regional topography.

Model: We model the uplift of the rift flanks as the flexural response of a thin elastic plate overlying a fluid substratum [8]. We assume that the flexure is of the form

$$w = \exp\left(\frac{-x}{\alpha}\right) \left[A \cos\left(\frac{-x}{\alpha}\right) + B \sin\left(\frac{-x}{\alpha}\right) \right] \quad (1)$$

where w is the vertical deflection of the plate from the regional datum, x is the distance along the profile, and α is the flexural parameter given by

$$\alpha = \left[\frac{E T_e^3}{3 \rho_m g (1 - \nu^2)} \right]^{1/4} \quad (2)$$

where E is Young's Modulus (60 GPa), T_e is the elastic plate thickness, ρ_m is the mantle density (3300 kg m^{-3}), g is the gravitational acceleration (8.87 m s^{-2}), and ν is Poisson's ratio (0.25). The objective is to find the three parameters A , B , and α such that the root-mean-square (rms) misfit between the observed and calculated topographic profiles is a minimum. Since w depends nonlinearly on α , we first fix the value of α , then calculate the best-fitting values of A and B . The flexural parameter is then varied over a range corresponding to an elastic plate thickness of 1 to 50 km, and the procedure is repeated. From the parameters providing the best overall fit we calculate the plate curvature at the first zero-crossing. This curvature and the apparent elastic plate thickness are then used to estimate the thermal gradient from the curves in [3].

We model only the rift flanks, so we remove the central rift depression from the profiles and model each rift flank separately. The location of highest topography in the half profile defines the origin of the horizontal axis. We fit topography up to 350 km from the rift, to avoid modeling the small rise 400 km to the south of the rift (Figs. 1 and 2). We also remove the mean elevation and the best-fit linear trend from our profiles before fitting to prevent bias from long-wavelength regional topography.

Results: Of the 14 profiles obtained in orbits 965–968 and 971–972, we analyze 10 that have flanks rising 600–1200 m above the regional mean elevation. Four of these profiles are well fit by elastic plate thicknesses of 8–16 km. For each of these profiles, there

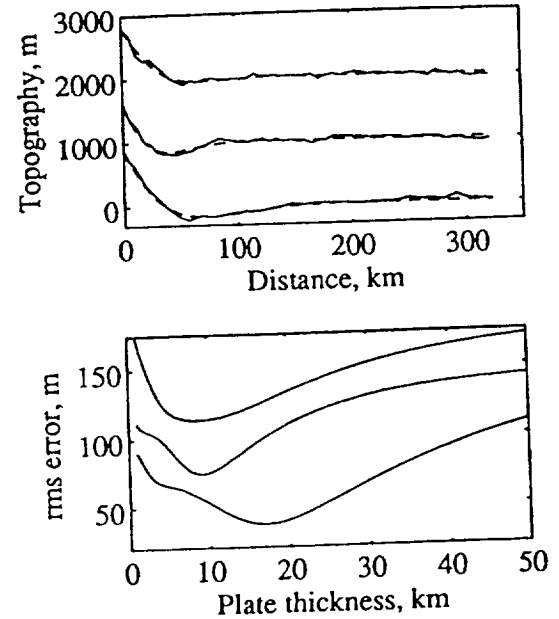


Fig. 3. Top: Topographic profiles (solid) and best-fit flexural profiles (dashed) for three half profiles; top to bottom are orbit 967, southern flank; orbit 968, southern flank; orbit 968, northern flank. Bottom: the rms error as a function of elastic plate thickness for the same profiles. Note that the top two profiles are best fit only over a small range of elastic plate thicknesses, whereas the bottom profile can be fit by a broader range of plate thicknesses. All profiles are consistent with elastic plate thicknesses in the range 8–20 km. For clarity, the upper two profiles at top have been vertically offset by 1000 m and 2000 m, respectively, and the corresponding error curves by 30 and 60 m.

is a narrow range of plate thicknesses for which the rms error is small, so the results are well constrained (Fig. 3). Three of these profiles produce best-fitting plate thicknesses of 8–9 km, suggesting that the true effective elastic plate thickness may be near the low end of this range. The remaining profiles generally contain more small-scale topographic variation of $\pm 100 \text{ m}$ in amplitude and are equally well fit by a range of plate thicknesses. The fits for all profiles, however, are consistent with elastic plate thicknesses of 8–20 km.

These effective plate thicknesses and the calculated curvatures imply thermal gradients of $15\text{--}30 \text{ K km}^{-1}$ if the base of the mechanical lithosphere is limited by the ductile strength of olivine [3]. Because the values of elastic lithosphere thickness derived here are comparable to or less than the estimated crustal thickness beneath plains regions on Venus [9,10], the base of the mechanical lithosphere may lie within the crust and be limited by the flow law for lower crustal material. In such a situation, the thermal gradients would be less than the figures given above.

The effective elastic plate thicknesses we derive for the Juno rift structure (8–20 km) are comparable to those obtained for the North Polar Plains at Uorsar Rupes (11–18 km) and both regions involve flexure of the lithosphere beneath plains at elevations near the planetary mean. A general relationship between regional elevation and elastic plate thickness might be expected if regional elevation were controlled by lithospheric thermal structure [11], as in the

Earth's oceanic regions. Further analysis of flexure is warranted to determine if such a relationship holds for Venus.

- References: [1] Solomon S. C. and Head J. W. (1982) *JGR*, 87, 9236. [2] McNutt M. K. (1991) *JGR*, 89, 11180. [3] Solomon S. C. and Head J. W. (1991) *GRL*, 17, 1393. [4] Sandwell D. T. and Schubert G. (1992) *JGR*, in press. [5] Sandwell D. T. and Schubert G. (1992) *Science*, submitted. [6] Weissel J. K. and Kerner G. D. (1989) *JGR*, 94, 13919. [7] Stofan E. R. (1992) *JGR*, in press. [8] Turcotte D. L. and Schubert G. (1982) *Geodynamics*, 125-131. [9] Grimm R. E. and Solomon S. C. (1988) *JGR*, 93, 11911. [10] Zuber M. T. and Parmentier E. M. (1990) *Icarus*, 85, 290. [11] Morgan P. and Phillips R. J. (1983) *JGR*, 88, 8305.

N93-14315

UNDERSTANDING THE VARIATION IN THE MILLIMETER-WAVE EMISSION OF VENUS. Antoine K. Fahd and Paul G. Steffes, School of Electrical Engineering, Georgia Institute of Technology, Atlanta GA 30332, USA.

Recent observations of the millimeter-wave emission from Venus at 112 GHz (2.6 mm) have shown significant variations in the continuum flux emission [1] that may be attributed to the variability in the abundances of absorbing constituents in the Venus atmosphere. Such constituents include gaseous H_2SO_4 , SO_2 , and liquid sulfuric acid (cloud condensates). Recently, Fahd and Steffes [2,3] have shown that the effects of liquid H_2SO_4 and gaseous SO_2 cannot completely account for this measured variability in the millimeter-wave emission of Venus. Thus, it is necessary to study the effect of gaseous H_2SO_4 on the millimeter-wave emission of Venus. This requires knowledge of the millimeter-wavelength (MMW) opacity of gaseous H_2SO_4 , which unfortunately has never been determined for Venus-like conditions.

We have measured the opacity of gaseous H_2SO_4 in a CO_2 atmosphere at 550, 570, and 590 K, at 1 and 2 atm total pressure, and at a frequency of 94.1 GHz. Our results, in addition to previous centimeter-wavelength results [4], are used to verify a modeling formalism for calculating the expected opacity of this gaseous mixture at other frequencies. This formalism is incorporated into a radiative transfer model to study the effect of gaseous H_2SO_4 on the MMW emission of Venus.

Experimental Configuration: The experimental setup used to measure the MMW opacity of gaseous H_2SO_4 atmosphere consists of a free-space transmission system as shown in Fig. 1. In this system, a glass cell contains the H_2SO_4/CO_2 gaseous mixture that is introduced prior to the measurement process. The glass cell is located inside a temperature-controlled chamber. A transmitting antenna is used to launch energy into the glass chamber. A receiving antenna is placed at the output of the glass cell in order to collect the outgoing signal. Using a precision variable attenuator, the resulting opacity of the gaseous mixture is measured.

Measurement Results: The measured absorptivity (dB/km) of H_2SO_4 at 94.1 GHz is shown in Fig. 2 where it is plotted as a function of temperature for 2 and 1 atm. The reported absorptivities in Fig. 2 are normalized to their respective mixing ratios. The measurements were performed at 550, 570, and 590 K in order to allow enough H_2SO_4 vapor pressure in the glass cell.

Although the measurements were performed at 94.1 GHz, care must be taken when projecting the absorption of H_2SO_4 at frequencies far from 94.1 GHz. As a result, we have developed an absorption model based on a Van Vleck-Weisskopf (VW) formalism. In this formalism, we added the contributions from 2359 resonant lines of H_2SO_4 computed by Pickett et al. (private communication, 1991) that cover frequencies between 1.5 and 450 GHz.

In order to fully implement the VW formalism, an appropriate broadening parameter must be determined. To solve this problem,

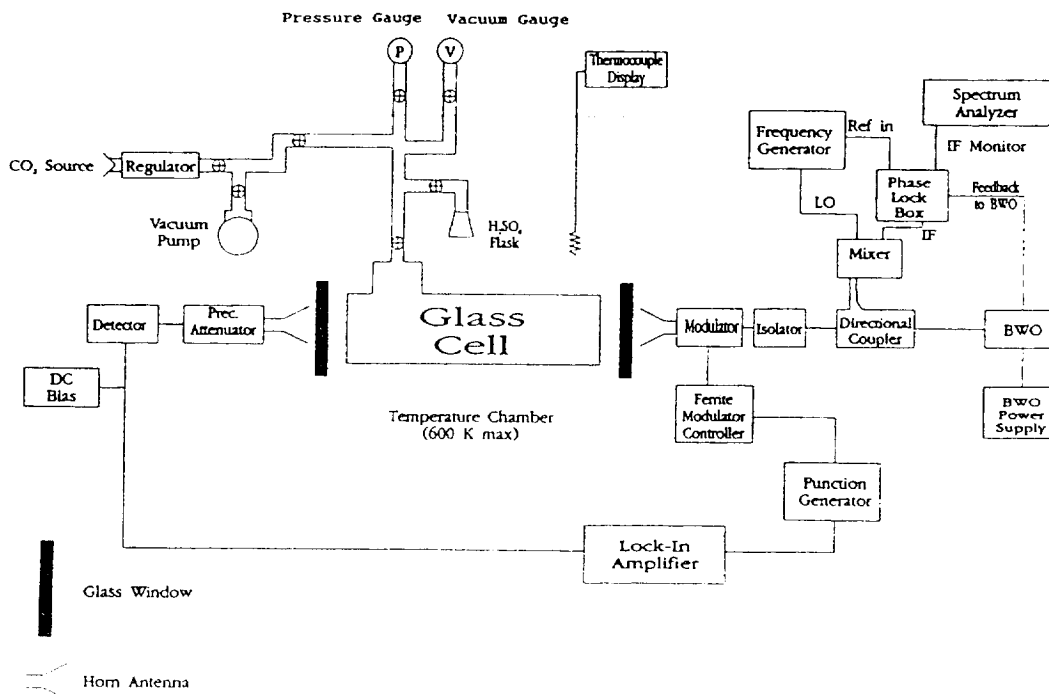


Fig. 1. Block diagram of the atmospheric simulator as configured for measurements of the millimeter-wave absorption at 94.1 GHz.